Cite this: *Soft Matter*, 2011, **7**, 5697

www.rsc.org/softmatter

PAPER

Formation and structure of slightly anionically charged nanoemulsions obtained by the phase inversion concentration (PIC) method†

Peggy Heunemann,*[ab] Sylvain Prévost,[ac] Isabelle Grillo,[b] Christina Michelina Marino,[d] Jürgen Meyer[e] and Michael Gradzielski*[a]

Received 30th December 2010, Accepted 30th March 2011
DOI: 10.1039/c0sm01556c

While nanoemulsions (10–200 nm) are not thermodynamically stable systems they can exhibit quite long term stability. In this paper oil/surfactant mixtures, containing diethylhexyl carbonate/phenoxyethanol/parabens as oil and polyglyceryl-4 laurate/dilauryl citrate as surfactant, form nanoemulsions simply by dilution with water, *i.e.* by means of the phase inversion concentration (PIC) method. In order to study this highly interesting phenomenon an investigation at constant oil-to-surfactant (*O*/*S*) ratio was done by means of viscosity, conductivity, and UV/Vis-transmittance measurements. This phase study as a function of the dilution by water shows that at an intermediate water content a two-phase system of bicontinuous structure is formed, which exhibits a very pronounced viscosity and conductivity maximum shortly before the homogeneous nanoemulsion phase is reached. In the same region SANS shows a high degree of ordering of this bicontinuous structure. SANS and cryo-TEM investigations of the nanoemulsion regime show an increasing average size with dilution and, more interestingly, the presence of two populations with different average particle sizes around 10–15 nm and 25–40 nm. The relative proportion of each population depends on the amount of added water, leading to an average growth of the particle size with increasing dilution.

1. Introduction

The surfactant aided dispersion of oil in water (or *vice versa*) often leads to the formation of more or less stable emulsions, where the size of the dispersed droplets is typically in the range of 0.1–10 μm.[1] They are thermodynamically unstable, *i.e.* will lead to macroscopic phase separation, where the time for this process to take place depends largely on the quality of kinetic stabilisation provided by the surfactant.[2] However it is also possible to form smaller sized emulsions in the size range of 10–200 nm, the so-called nanoemulsions.[3–5] They often exhibit remarkably high kinetic stability, being relatively stable against coalescence and Ostwald ripening,[2] which renders them interestingly for a variety of applications.[6] Of course, in general nanoemulsions are prone to Ostwald ripening but their frequent long-time metastability indicates that this process is often effectively slowed down. In addition, due to their small size they are intrinsically stable against creaming or sedimentation.[7] Typically such nanoemulsions are produced by high-energy input methods, such as high-pressure homogenisation or ultrasonic treatment.[8–14] However, apart from being energy intensive such methods could also be damaging for sensitive ingredients (*e.g.* biomolecules, active agents, drug molecules, *etc.*) incorporated in such formulations.

Therefore a highly interesting approach to produce such finely dispersed emulsions is by means of low energy input methods, which is very appealing both from a fundamental scientific point of view but also for many applications, where nanosized dispersions of an oil in water or *vice versa* shall be achieved by a simple preparation method. Classically this can be done by means of employing the method of the phase inversion temperature (PIT),[15–18] where typically one starts from a water-in-oil (W/O) microemulsion at high temperature and enters into a long time stable oil-in-water (O/W) nanoemulsion below the PIT by a rapid cooling process. More recently an analogous strategy has been devised by the phase inversion concentration (PIC) method.[19–23] In particular, the PIC method is very appealing from a practical point of view as it only involves a simple dilution with a solvent (typically water) to produce the nanoemulsion.

[a]*Stranski-Laboratorium für Physikalische und Theoretische Chemie, Institut für Chemie, Technische Universität Berlin, D-10623 Berlin, Germany. E-mail: michael.gradzielski@tu-berlin.de; Fax: +49 30 314 26602; Tel: +49 30 314 23931*

[b]*Institut Max von Laue-Paul Langevin (ILL), F-38042 Grenoble, France. E-mail: grillo@ill.fr; heunemann@ill.fr; Fax: +33 4 76 20 71 20; Tel: +33 4 76 20 70 63*

[c]*Helmholtz-Zentrum Berlin für Materialien und Energie GmbH, D-14109 Berlin, Germany. E-mail: sylvain.prevost@helmholtz-berlin.de; Fax: +49 30 8062 42523; Tel: +49 30 8062 42339*

[d]*Department of Chemical Engineering, DE-19716, USA. E-mail: crusso@udel.edu*

[e]*Evonik Goldschmidt GmbH, Consumer Specialties, D-45127 Essen, Germany. E-mail: juergen.meyer_dr@evonik.com; Fax: +49 201 173 1857; Tel: +49 201 173 1621*

† Electronic supplementary information (ESI) available. See DOI: 10.1039/c0sm01556c

However, so far especially for the PIC method a systematic understanding about how to choose and optimise oil/surfactant systems that work efficiently has not yet been achieved. Often it is claimed that passing through a lamellar phase or the vicinity of it in the process of nanoemulsion formation is a necessary prerequisite for the spontaneous formation of stable nanoemulsions as it has been established for the PIT method.[16] Similar indications were given for the PIC method.[24] However, in general the PIT method has been studied in much more detail than the PIC method. Up to now various oil/surfactant mixtures are known to form nanoemulsions spontaneously upon dilution with water, *e.g.* Span and Tween surfactants mixed with decane,[25,26] potassium oleate/$C_{12}E_{10}$ and hexadecane,[27] or oleylammonium chloride/oleylamine/$C_{12}E_{10}$ and hexadecane.[28] However, up to date there is no systematic knowledge regarding the molecular composition of the oil/surfactant combinations required to successfully obtain a nanoemulsion. Accordingly one is in the uncomfortable situation that finding them occurs mostly by serendipity and not in a systematic fashion based on a thorough understanding of the criteria that allow for their formation. In this article we will be concerned with the structural details of the formation process of nanoemulsions and some aspects relevant for their stability, which are still poorly understood. A primary aim of our investigation therefore is to learn how one may understand the formation of nanoemulsions in such systems with a particular emphasis on the structures formed.

Our studies are based on a commercially available oil/surfactant (O/S) mixture, consisting of diethylhexyl carbonate, phenoxy ethanol, polyglyceryl-4 laurate and dilauryl citrate (Tego® Wipe DE). The system has been described previously[29] and forms O/W-nanoemulsions at a certain oil/water ratio, presumably due to the change of interfacial composition during dilution.

The aim of our study was to extend this phenomenological study in a more systematic and comprehensive way, in order to understand nanoemulsion formation by the PIC method from a fundamental point of view. For that purpose we studied the overall phase behaviour as a function of the addition of water, complemented by measurements of the electric conductivity and viscosity. Particular emphasis was given to a detailed mesoscopic structural characterization of the PIC system and its structural evolution over the full range of dilution. Accordingly in our investigation we varied the oil/water-ratio concentration on the transitional composition range, *i.e.* dilutions less than those required to form nanoemulsions, and the more dilute region of the nanoemulsions. For that purpose the structure was determined by means of turbidity measurements, small-angle neutron scattering (SANS) and cryogenic-transmission electron microscopy (cryo-TEM).

2. Materials and methods

2.1 Materials

The basic oil/surfactant (O/S) composition (TEGO® Wipe DE (Evonik Goldschmidt)) consists of ~66 wt% diethylhexyl carbonate (TEGOSOFT® DEC (Evonik Goldschmidt)), ~12 wt % of a preservative mixture consisting of phenoxyethanol (main component (72 wt%)) and different parabens (methyl- (16 wt%), ethyl- (4 wt%), propyl- (2 wt%), butyl- (4 wt%) and isobutylparabene (2 wt%)), and 22 wt% polyglyceryl-4 laurate (TEGO® Care PL 4 (Evonik Goldschmidt)) (Fig. 1) containing a small amount (~0.9 wt%) of dilauryl citrate as surfactants. It should be noted that at the given pH of 5.5–6 of the solutions the citrate is fully charged and contains one charge per surfactant molecule.

All components were obtained as gifts from Evonik Industries. Water was deionised and further treated by Milli-Q purification. D_2O for SANS-measurements was purchased from Euriso-top (99.85%D).

2.2 Methods

2.2.1 Preparation. Nanoemulsions and samples at lower water content were prepared by a one step dilution of oil/surfactant mixtures. The formation process was typically initiated by vortex mixing but could also be done by simple hand mixing. The way of mixing (single-step or step-wise addition of oil or water; vortex or hand mixing) did not affect the final structure or behaviour. To achieve metastable O/W-nanoemulsions the water concentration had to be higher than 75 wt%. Nanoemulsions appear as milky/white turbid, water viscous solutions with a more bluish or reddish tint depending on the angle of the incident light and dispersed droplet size (the lower the water content the more bluish the solutions). Flow birefringence was checked using polarisers while shaking the sample gently.

The age of the samples, as well as that of the starting formulation of the surfactant/oil is relevant as ageing is an important issue in these systems and was always carefully registered. Measurements that are compared were always done on samples of identical age.

2.2.2 Electric conductivity. For assigning the type of emulsion (*i.e.* water continuous or not), conductivity measurements were done. The electrical resistance was measured at a constant temperature (25.0 ± 0.1 °C) using a conductometer 712 by Metrohm. In biphasic regions the previously separated phases were measured individually, provided adequate volumes (>~25 vol%) were available. The given conductivities are averaged values of four repeated measurements.

2.2.3 Interfacial tension. Interfacial tension measurements were done at 25.0 ± 0.1 °C by means of a spinning drop tensiometer (Krüss—SITE 04), using water as a continuous phase.

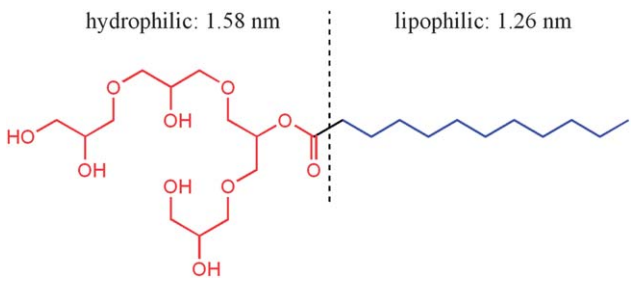

Fig. 1 Structure of the main surfactant polyglyceryl-4 laurate; its stretched molecular length is 2.84 nm (*left*: hydrophilic part (1.58 nm); *right*: lipophilic part (1.26 nm)).

2.2.4 Viscosity. For measuring the kinematic viscosity of the Newtonian fluids, calibrated Ubbelohde capillary viscosimeters (Schott) were used at a constant temperature (25.0 ± 0.1 °C). The kinematic viscosity ν was measured ten days after preparation, by determining the capillary suction time t of a given volume (V = 20 mL), at a defined cross-section (radius r), *via* the Hagen–Poiseuille equation and taking into account the Hagenbach–Couette correction ζ (eqn (2)), that accounts for the difference between theoretical and measured flow time due to the drop in pressure by fluid acceleration at the capillary entrance. Here, K is a device-specific constant, given by certified calibration measurements of Schott (model: 0a (ν = 0.8–5 mm^2 s^{-1})/I (ν = 1.2–10 mm^2 s^{-1})/I_c (ν = 3–30 mm^2 s^{-1})), and η, the dynamic viscosity, which is connected *via* the sample density ρ with the kinematic viscosity ν (eqn (1)).

$$\nu = \frac{\eta}{\rho} = K(t - \zeta) \tag{1}$$

$$\text{with } \zeta = \frac{0.00168\sqrt[3]{V}}{l\sqrt{2r}\sqrt[3]{K}t^2} \tag{2}$$

The flow time t was registered automatically by Viscoboy 2 (MWG Lauda). The given viscosities are averaged values of five consecutive measurements.

2.2.5 UV-vis transmittance and turbidity measurements. The dilution process of the Tego® Wipe DE formulations was followed with a Clariant Cary 50 Tablet UV/VIS instrument, ten days after preparation at 25.0 ± 0.1 °C, using Hellma cuvettes of 1 or 10 mm thickness—depending on transmittance. Using the obtained transmissions T the turbidity coefficient τ was calculated according to eqn (3):

$$\tau = -\frac{\ln T}{d} \tag{3}$$

where d is the thickness of the cuvette. In the biphasic region phase separated measurements were accomplished for phases with adequate (>∼25 vol%) volumes of the individual phases.

In the nanoemulsion region (water conc. >75 wt%) the spectra (350–800 nm) were measured in 0.5 mm Hellma cuvettes in order to avoid multiple scattering effects. Measurements were done with a Jasco-V630 photometer at 25.0 ± 0.1 °C. All measurements were done ten days after preparation.

In both cases the signal of a water filled cuvette was subtracted to get the spectrum of the sample.

2.2.6 Small-angle neutron scattering (SANS). All samples for SANS experiments were prepared by adding appropriate D_2O volumes to the oil phase at room temperature as described above for the H_2O-case and stored for ten days in a bath thermostatted at 25.0 ± 0.1 °C before measuring them at the same temperature. D_2O was used instead of H_2O to increase the contrast and lower the incoherent background, accounting for the density difference, thereby keeping volumetric and molar compositions identical to the corresponding H_2O samples. For biphasic samples both phases were measured separately. Plots of SANS results, that are depicted as a function of D_2O-content, refer to the corresponding volume fraction of H_2O. SANS measurements were done on D22 at Institut Laue Langevin (ILL), Grenoble, France. Spectra were recorded on a 2-dimensional gas detector of 128 × 128 pixels of 8 × 8 mm^2. The wavelength was 8 Å (FWHM 10%) and sample-to-detector distances of 1.4, 5, and 17 m were selected to cover a wide range of the wave vector magnitude q = 0.03–5 nm^{-1}, where $q = 4\pi\sin(\varphi/2)/\lambda$ with φ being the scattering angle. Collimation lengths of 5.6, 8, and 17.6 m were chosen, respectively. Samples were kept in quartz cuvettes of QS quality (Hellma) of 1 mm path length, which were placed in a thermostatted (25.0 ± 0.1 °C) sample-changer.

Raw data were corrected for the scattering of the empty cell. The pixel efficiency and solid angle variation were taken into account by dividing with the scattering pattern of pure water in a 1 mm cuvette. The background noise was accounted by measurements with boron carbide (B4C) at the sample position. The absolute scale was determined by the transmission of the water, assuming the ideal case where non-transmitted neutrons are scattered uniformly over the full solid angle of 4π and considering the Jacrot factor (for 8 Å: 1.089) that accounts for the wavelength dependent forward scattering of water.[30] The reduced data obtained using BerSANS[31] were always isotropic and consequently azimuthally averaged. Spectra from different configurations for each sample were merged with no need of any scaling factor. The presented SANS curves still contain the incoherent background scattering of the solvent and the sample.

2.2.6.1 Scattering theory-model independent methods. The scattering length densities (SLDs) used in this work[32] are displayed in Table 1.

For the range of $qR < 1$, the Guinier approximation can be employed according to which for the presence of individual, non-interacting particles the scattering intensity $I(q)$ depends only on the radius of gyration, R_G (eqn (4)).[33] For emulsion droplets, an average sphere radius R can be obtained by the relation: $R_G^2 = 3/5R^2$ (as in D_2O they can to first order be considered as being homogeneous).

$$\ln I(q) = \ln I(q = 0) - \frac{R_G^2}{3}q^2 + I_{bkg} \tag{4}$$

However, the average particle size R can also be approached by using the extrapolated zero-angle intensity I (q = 0), which is given by the contrast ΔSLD (the difference between the scattering length densities of the particle and the matrix), the volume fraction Φ, and the volume of one scattering particle V_p, which can simply be used to calculate the radius of the corresponding sphere.

$$\ln I\,(q = 0) = \Phi V_p S(0)\Delta\text{SLD}^2 \tag{5}$$

$$R = \sqrt[3]{\frac{3}{4}\frac{I_0}{\pi\Phi\Delta\text{SLD}^2}} \tag{6}$$

It should be noted that for polydisperse systems the averages obtained for R differ, as by the Guinier analysis a z-average is obtained, while the value from I (q = 0) is a M_w-average. Accordingly the latter should always be somewhat smaller.

The invariant Q is a fundamental result of scattering theory,[34] which states that independently of the structure of the system (shape, size, interactions), in a two-phase system its value

Table 1 Sum formula, densities ρ, weight fraction wt% and scattering length densities (SLDs) of the individual components of the oil/surfactant formulation

	Formula	ρ^{25}/g cm^{-3}	Wt%	SLD/10^{-6} Å^{-2}
Deuterium oxide	D_2O	1.1072		6.37
Phenoxyethanol	$C_8H_{10}O_2$	0.9540	12	1.32
Diethylhexyl carbonate	$C_{17}H_{34}O_3$	0.8925	66	0.061
Polyglyceryl-4 laurate	$C_{24}H_{48}O_{10}$	1.0944	21.1	0.505
Dilauryl citrate	$C_{30}H_{56}O_7$	1.0110	~0.9	0.353

depends only on the volume fraction Φ and the scattering contrast ΔSLD.

$$\bar{Q}_{\text{theo,homo}} = 2\pi^2\Phi(1-\Phi)\Delta\text{SLD}^2 \tag{7}$$

The experimental invariant can be obtained by calculating the integral,

$$Q_{\text{exp}} = \int_{q=0}^{\infty} I(q)q^2\text{d}q \tag{8}$$

extrapolating the experimental data to zero and infinity scattering vector q. However, for our experimental data, using, respectively, the Guinier and Porod approximation, which require in particular that intensity reaches or comes close to a plateau with the experimental low q region, both extrapolations to low and high q provided an empirical invariant which is in a good agreement to the theoretical one, with an error estimate of approx. ±15% ($\Delta Q_{\text{extrapolation}}$ = 10%; ΔQ_{data} = 5%). Differences between experimental and theoretical invariant would indicate a molecular dissolution of components.

2.2.6.2 Scattering theory—Teubner–Strey model. A very useful model which is often used for the characterization of bicontinuous microemulsions is the Teubner–Strey approximation, which is based on Landau's free energy theory and Debey–Anderson–Brumberger's derivation of scattering by inhomogeneous domains.[35,36] The scattering intensity is described by eqn (9), where $\langle\eta\rangle \equiv \Phi_O\Phi_W\langle\Delta\text{SLD}^2\rangle$ and $\langle\Delta\text{SLD}^2\rangle$ is the difference in scattering length density between oil (o) and water (w). a_2, c_1 and c_2 are coefficients of various terms of order parameters in Landaus free energy. In the case of a microemulsion, c_1 indicates the tendency to form interfaces between different domains and is usually negative, whereas a positive a_2 favours the microemulsion formation. For a stable morphology the criterion of $4a_2c_2 - c_1 > 0$ with a positive c_2 is required.[35]

$$I(q) = \frac{8\pi c_2\langle\eta^2\rangle/\xi_i}{a_2 + c_1q^2 + c_2q^4} \tag{9}$$

$$\gamma(R) = \frac{\sin(\varepsilon R)}{\varepsilon R}\exp\left(-\frac{R}{\xi_i}\right) \tag{10}$$

The corresponding correlation function is given by eqn (10) and incorporates alternating regions of water and oil domains with $\varepsilon = 2\pi/D_s$ giving the quasiperiodic repeat distance (periodicity) D_s (eqn (12)). D_s can be associated with a peak in the SANS spectra at $2\pi/D_s$ in the case of high densities and order. The number density ^1N is given *via* the volume fraction through $^1N = \Phi/V = 1/D_s^3$ in the case of a simple cubic packing assumption. Hence the correlation length can also be extracted from SANS data as:

$$\xi_i = \frac{\pi}{Q}\int I(q)q\text{d}q \tag{11}$$

The correlation length ξ_i (eqn (13)) corresponds to a characteristic length for positional correlation, *i.e.* related to a characteristic size of the structural domains contained.

$$D_s = 2\pi\left[\frac{1}{2}\sqrt{\frac{a_2}{c_2}} - \frac{1}{4}\frac{c_1}{c_2}\right]^{-1/2} \tag{12}$$

$$\xi_i = \left[\frac{1}{2}\sqrt{\frac{a_2}{c_2}} + \frac{1}{4}\frac{c_1}{c_2}\right]^{-1/2} \tag{13}$$

To describe the degree of ordering in nano- or microemulsions the amphiphilicity factor f_a given by eqn (14)[37,38] can be used, as demonstrated previously for bicontinuous microemulsions.[39,40]

$$f_a = \frac{c_1}{(4a_2c_2)^{1/2}} \tag{14}$$

The range of f_a reaches from 1 for a completely disordered solution to −1 for a superlattice which assumes in the case of microemulsions a lamellar structure. When the Lifschitz line is crossed at $f_a = 0$ a peak at non-zero wave vector can be observed. Therefore the amphiphilicity factor provides a useful scale for the quantification of the extent of ordering.[41]

2.2.6.3 Scattering theory—polydisperse sphere model with log-normal distribution. For emulsion systems containing homogeneous spheres, the form factor $F_{\text{HS}}(q)$ is given by eqn (15) through the magnitude of the scattering vector q, the sphere radius R and the difference in scattering length density $\Delta\text{SLD} = \text{SLD}_{\text{sph}} - \text{SLD}_{\text{solv}}$ of the sphere and the solvent. In the case of polydisperse (pd) systems the form factor (eqn (16)) has to be averaged by a particle size distribution. This was done using a log-normal distribution $f(R,R_i,\sigma_i)$ (eqn (16)), where σ describes the polydispersity of a population.

$$F_{\text{HS}}(q,R) = 3\frac{4}{3}\pi R^3\Delta\text{SLD}\frac{\sin(qR) - qR\cos(qR)}{(qR)^3} \tag{15}$$

$$f(R,R_i,\sigma_i) = \frac{\exp\left(-\frac{\ln\left(R/u(R_i,\sigma_i)\right)^2}{2\nu^2(R_i,\sigma_i)}\right)}{\sqrt{2\pi}R\nu(R_i,\sigma_i)} \tag{16}$$

$$\text{with } u(R_i,\sigma_i) = \frac{R_i^2}{\sqrt{\sigma^2(R_i,\sigma_i) + R_i^2}}$$

$$\nu(R_i,\sigma_i) = \sqrt{\ln\left((\sigma(R_i,\sigma_i)/R_i)^2+1\right)}$$

$$\text{and } \sigma(R_i,\sigma_i) = R_i\sigma_i$$

The total scattering intensity of a polydisperse homogeneous spherical particle can be described hence by eqn (17), where ^1N ($=N/V$) is the number density of particles and I_{Bkg} the incoherent background scattering.

$$I_{HS}(q) = \left(\frac{4\pi}{3}\right)^2 {}^1N\Delta SLD^2 \int_0^\infty f(R, R_0, \sigma_0) R^6 {F_{HS}}^2(q, R) dR + I_{Bkg} \quad (17)$$

In the case of a bimodal log normal distributed spherical model (BHS) a linear combination of both populations leads to eqn (18). Φ is the volume fraction of the particles, whereas A refers to the volume fraction of the scattering material that is in the species with radius R_1 and $(1 - A)$ to the species of radius R_2.

$$I_{BHS}(q) = \left(\frac{4\pi}{3}\right)^2 {}^1N\Delta SLD^2 \left[\int_0^\infty A f(R, R_1, \sigma_1) R^6 {F_{HS}}^2(q, R) dR + \int_0^\infty (1 - A) f(R, R_2, \sigma_2) R^6 {F_{HS}}^2(q, R) dR \right] + I_{Bkg} \quad (18)$$

The experimental smearing (mostly determined by the spread of wavelength which in our case was given by a FWHM of 10%) was considered within the distribution function and the values given therefore refer directly to the polydispersity of the particles. Interparticle interferences were accounted for by a hard-sphere structure factor with a fixed hard-sphere radius of ~39 nm.[42]

Beside the data treatment with mono- and bimodal polydisperse spherical models, we also employed the identical polydisperse model for a core–shell form factor, thereby accounting for the slight differences in scattering length density between the surfactant shell and oil. However, this model did not yield substantially improved fits of the experimental data and also had no systematic impact to the final fit parameters. Therefore in the following we will just give the data obtained from the homogeneous spherical model.

2.2.7 Cryogenic transmission electron microscopy (cryo-TEM). Oil in water (o/w) samples were prepared as described above and arranged on Quantfoil carbon-coated copper grids with a 200 mesh. Grid samples were prepared in a Vitrobot machine by FEI Company™ (Tools for Nanotech). The grid was suspended between a pair of tweezers in a chamber with controlled temperature (25.0 ± 0.1 °C) and humidity (100% humidity), where it was then dipped into a vial with the sample. The tweezers were then pneumatically lifted from the sample to an area between two blotting papers where the grid was blotted automatically with a specified time of blotting and number of blots. After a given relaxation time, the grid was immediately plunged in liquid ethane where it was vitrified at the freezing point of ethane (−165 °C). The specifications of the blotting parameters were 2 blots held at 1 second for each blot, and the grid was allowed to relax in the chamber after blotting for 30 seconds. The blotting paper was kept at a −1 offset where a positive offset gives a softer blot and a negative offset gives a harder blot. The sample was then viewed in a FEI Tecnai G2 12 twin transmission electron microscope at a voltage of 120 kV. The sample was kept at −175 °C or lower with a Gatan 626 cryo-specimen holder. The images were digitally recorded with a Gatan 794 CCD camera at about 12 micrometres of underfocus.

3. Results and discussion

3.1 Phase behaviour

As a first step we characterised the phase behaviour of the surfactant/oil mixture as a function of the added amount of water at 15.0, 25.0, and 40.0 ± 0.1 °C which is depicted in Fig. 2.

It should be denoted that the phase characterisation given here does not refer to a proper phase diagram, because of the metastable properties of nanoemulsions. Therefore the "phases" depicted here are not really thermodynamically stable, but instead just more or less long time metastable states. Accordingly the samples were inspected after 2 and 10 days thereby giving the appearance of the samples at time scales relevant to our experiments. However, it should always be kept in mind that, depending on the location in the phase diagram, samples could still be evolving and changing substantially with time. In fact this can also be seen in the shift of the multiple phase regions that become larger with temperature and time, which can be attributed to the already mentioned metastability of nanoemulsions. Whereas the influence of temperature is larger than the time-dependence, both are controlling ageing processes like coalescence and Ostwald ripening. However, at room temperature and below these processes are slowed down.

Addition of water to the oil phase leads at first (<10% H_2O) to a complete incorporation of the water by the surfactant/oil mixture *via* molecular dissolution, forming a clear, slightly bluish inverse microemulsion (Fig. 2 and 8). At higher water content the system becomes biphasic, containing the initial microemulsion in an upper phase (becoming more turbid with increasing water content), and a lower clear water excess phase. Around 50 wt% water content, a microemulsion-like single phase is observed that shows macroscopic phase separation after several weeks (which might be due to chemical degradation of the citrate surfactant).

As a rule the higher the water content the slower is this process until a total amount of 60 wt% H_2O. The adjacent biphasic region at higher water content differs largely with respect to its visual appearance insofar as both phases appear bluish and are of similar turbidity (Fig. 3) (measurements of the separated phases were only performed when adequate volumes were available, *i.e.* above ~25% of the total volume).

Generally the upper phases are more turbid than the lower phases, and they become clearer with increasing water concentration. This happens until the phase inversion concentration (PIC) is reached (H_2O > 75%) and leads to single, slightly blue shining, milky nanoemulsions (NEs). As indicated in Fig. 3 further dilution until 90% H_2O enhances the turbidity strongly and can be correlated to the NE-evolution (see also Section 3.2.2). Additional dilution leads to a clearing of the nanoemulsion due to the decreasing volume fraction of the dispersed material. As already mentioned, before forming nanoemulsions, a more or less broad area of bluish microemulsions is passed in the H_2O-range of >55–78.5 wt%, that shows flow birefringence.

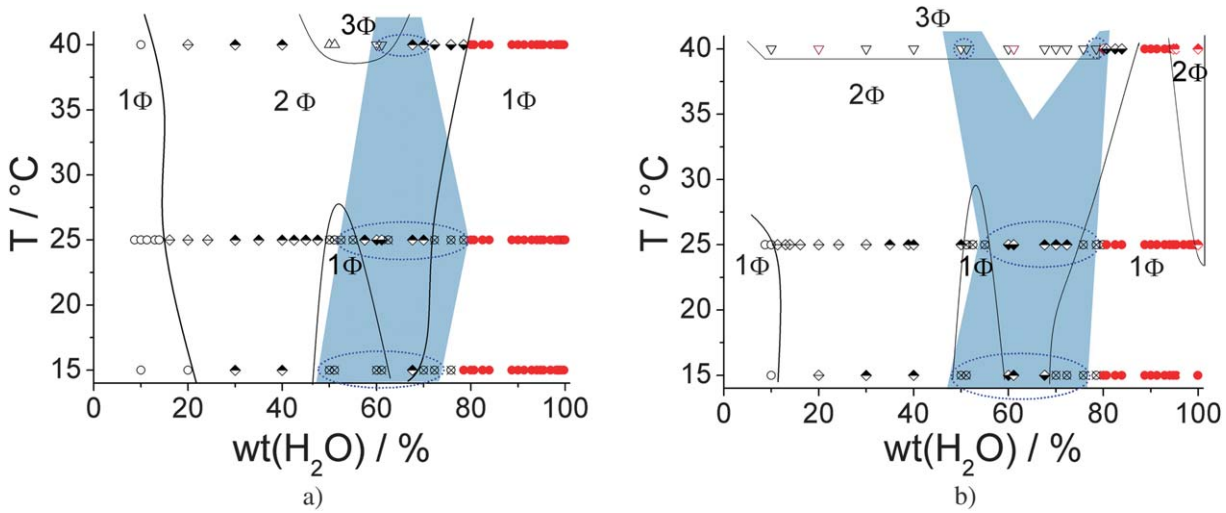

Fig. 2 Phase behaviour of the oil/surfactant mixture as a function of water concentration, at various temperatures (15.0, 25.0, 40.0 ± 0.1 °C) taken after 2 (a) and 10 (b) days of preparation, shaded areas showed flow birefringence—in biphasic case: observed in upper phase (1Φ: ○ clear, ⊗ μE, ● NE; 2Φ: ⟐ clear, ⬘ upper Φ, ⬙ lower Φ (more turbid); 3Φ: ▽).

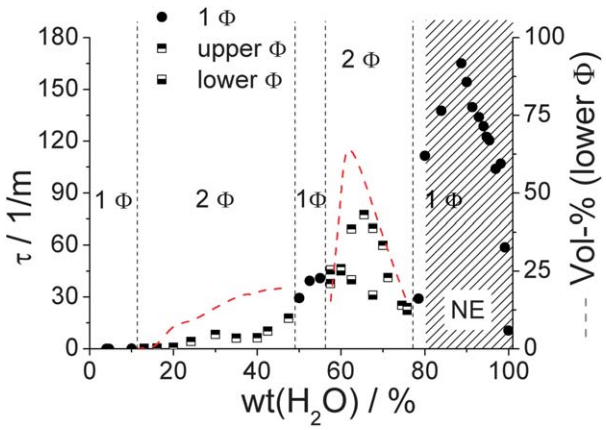

Fig. 3 Turbidity coefficient τ at 626 nm of the composition-dependent UV-VIS measurements (dots) for oil/surfactant mixtures as a function of water concentration and 25 ± 0.1 °C; and corresponding volume fraction (vol%) of the lower phases (dotted line) in the biphasic region (the shaded area is the nanoemulsion).

In that context it must be noted that this "1Φ NE" region is not a thermodynamically stable single phase region. After several months one will observe a macroscopic phase separation with an oil phase on top of the aqueous solution. This means that this system is an emulsion and due to its small size (see Section 3.2) a nanoemulsion by definition. However, the structural evolution occurs rather slowly as shown in Fig. S1† and apparently this nanoemulsion is kinetically very stable.

This flow birefringence (shaded area in Fig. 2) occurs in the single phases as well as in the upper phases of the biphasic samples and has either to be correlated to a non-spherical shape of the aggregates[43] or to the more likely presence of an L_3-phase.[44–46] In general, it has been found that nanoemulsions are frequently formed by passing a bicontinuous microemulsion or a liquid crystalline lamellar phase[24] during the preparation process and this observation has in particular been detailed for the case of the PIT method.[16,47,48] It should further be mentioned that for non-ionic surfactants also lamellar liquid crystals[49] and for ionic surfactants cubic liquid crystals[27] have been inferred to be relevant in order to yield robust nanoemulsions *via* the PIC-method (sometimes also referred to as Emulsion Inversion Point method, EIP method;[50] or Phase Inversion Composition method, PIC method[51]). All these structures have one characteristic in common in that they allow for a reversion of the sign of the curvature for the oil–water interfacial film. This phenomenon culminates in a complete overall structural inversion from having an oil-continuous system or *vice versa*, which then leads to the formation of nanoemulsion droplets in the dispersed phase. In parallel the interfacial tension between oil and water passes through a minimum thereby enabling the formation of very small emulsion droplets.[6]

Viscosity and conductivity measurements by Meyer *et al.*[29] of mixed solutions in the inhomogeneous region and our phase separated studies showed a similar behaviour when forming nanoemulsion by the PIC method compared to the PIT one.[52–54] For the case of PIT-nanoemulsions the formation process of nanoemulsions can be traced back to the change of solubility of polyoxyethylene-type surfactants (change of HLB value with temperature), whereas in the case of PIC-nanoemulsions the relative amount of surfactant present in the water phase increases with dilution, thereby modifying the composition of the amphiphilic monolayer at the oil/water interface (Fig. 4).

Both methods take advantage of the extremely low interfacial tension (10^{-2} to 10^{-6} N m^{-1} (ref. 55)) at the phase inversion temperature[17,18,56] or phase inversion concentration.[57–60] The value of the interfacial tension between the undiluted oil/surfactant mixture and water as a continuous phase was measured to be 0.0175 mN m^{-1}. This value is rather low and would be typical for microemulsion forming systems.[61]

However, in direct comparison, the first viscosity maximum at ~52.5 wt% (H_2O) (Fig. 5a) seems to indicate the transition of a droplet type to a bicontinuous microemulsion, as for classical microemulsions such a maximum of viscosity in the region of this

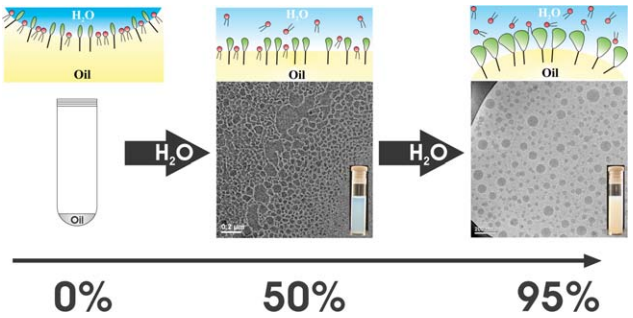

Fig. 4 Schematic depiction of the mechanism of phase inversion of the W/O-emulsion to O/W-nanoemulsion *via* passing of sponge like micro-emulsion phase with zero curvature; exemplify cryo-TEM images by C. M. Marino (UD, USA).

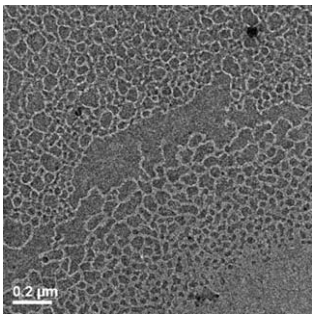

Fig. 6 Cryo-TEM image for a sample diluted to 50 wt% of water.

structural transition is typically observed.[62,63] The following biphasic area is caused by a morphological change that can refer to the bicontinuous structure and is accompanied by a typically viscosity minimum.[64] In the region of the viscosity maximum the electric conductivity (Fig. 5b) passes through a pronounced maximum which peaks exactly at the point where the system becomes monophasic. Both observations indicate the presence of a bicontinuous structure of high connectivity at the phase boundary. The bicontinuous structure of the single-phase region around 50 wt% (H_2O) was further corroborated by cryo-TEM images for which one example is shown in Fig. 6.

3.2 Structural characterisation

After having studied the more general aspects of macroscopic phase behaviour during stepwise nanoemulsion formation, we were then interested in determining the mesoscopic structure of the respective samples in order to establish a correlation between the structure and macroscopic phase behaviour. For this purpose we employed UV/Vis-spectroscopy, SANS, and cryo-TEM. Of course, our systems being metastable one has to worry about their changes as a function of time. For the case of the nano-emulsion range we ascertained by long-time turbidity measurements (see Fig. S1†) that no significant structural changes take place during our typical experimental time window of 2–5 days.

3.2.1 UV/Vis-transmittance measurements of nanoemulsion region. Turbidity measurements have been performed for nano-emulsions with oil/water ratios of 80, 85, 90, 95 and 98% H_2O (Fig. S2†). From the value of the turbidity τ we calculated the molecular weight M_w of the colloidal particles according to eqn (19)[65] and converted this value to obtain an approximate particle size R for spherical particles (eqn (20)).

$$M_w = \frac{\tau 3 N_{Av} \lambda^4}{32\pi^3 n^2 c_g (dn/dc_g)^2} \quad (19)$$

$$R(M_w) = \left(\frac{M_w}{(4/3)\pi\rho N_{Av}}\right)^{1/3} \quad (20)$$

$$a_h = \frac{3c_g}{c_S N_{Av} \rho R(M_w)} \quad (21)$$

Here N_{Av} is the Avogadro constant, λ the wavelength of light, n the refractive index of the solvent, c_g the mass concentration of the dissolved particles (assuming all surfactant and oil to be contained in the particles), dn/dc_g the refractive index increment, and ρ the density of the aggregates. Calculations have been done

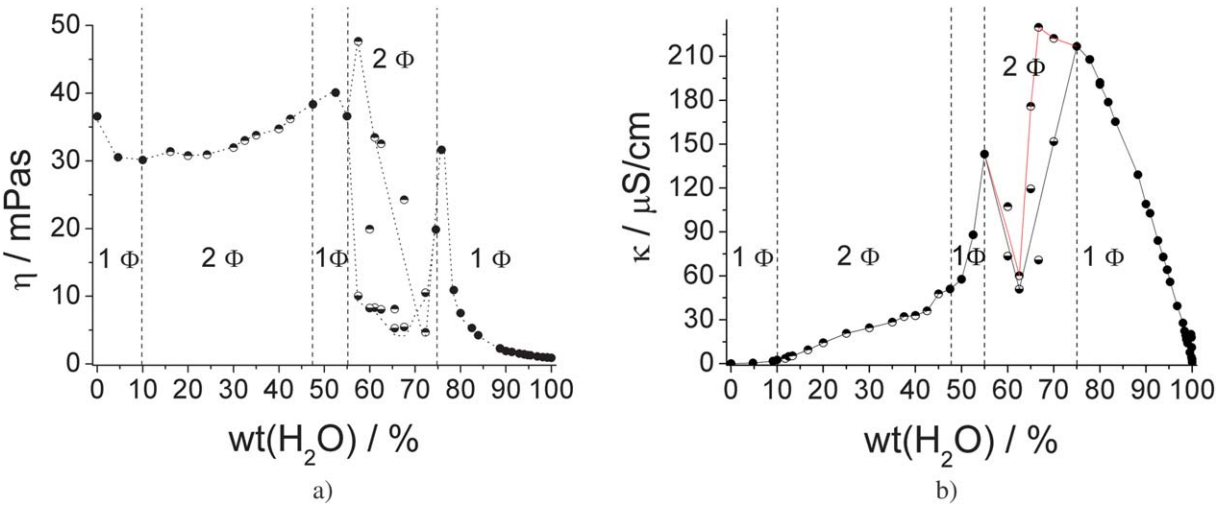

Fig. 5 Dynamic viscosity η (a) and electric conductivity κ (b) measurements as a function of water concentration (TW + H_2O) at 25 ± 0.1 °C in respect to biphasic regions (for adequate volumes >~25 vol%)—●: 1Φ; ◓: upper Φ; ◒: lower Φ.

for seven different wavelengths λ (350, 400, 500, 600, 626, 700, 800 nm), but we considered only transmission values above 80% and ascertained by comparing the values for different wavelengths that effects from multiple scattering were negligible (see also Table S3†). The results show good agreement for all wavelengths and the mean of the turbidity τ has been used to calculate the molecular weights M_w; particle sizes $R(M_w)$ of the oil droplets (Fig. 7) and the surfactant head group area a_h(S) (eqn (21)) are summarized in Table 2. For the calculation of the surfactant head group area a_h(S), c_S is the surfactant concentration.

The typical size of the nanoemulsion droplets is bigger than 20 nm, whereas the required space of the surfactant head groups a_h(S) is below 0.5 nm^2 (Table 2). The particle size increases with water concentration following a more or less linear relation (Fig. 7). This size increase with increasing dilution can be attributed to the fact that the relatively hydrophilic surfactant will become increasingly dissolved in the aqueous phase upon increasing dilution. Accordingly the average particle size of emulsion droplets formed has to increase. As the scattering intensity is size dependent one obtains a mass-average, *i.e.* in a broad distribution the bigger particles dominate the scattering. Of course, it must be stated here that these numbers have to be taken with a grain of salt, as in this analysis we completely neglect the fact that according to the proposed PIC mechanism a part of the oil/surfactant mixture should become dissolved into the water phase. Accordingly the real concentration c_g of dissolved aggregates should be smaller and therefore the radii and head group areas deduced have to be seen as lower and upper limits with respect to the real values, respectively. Therefore the rather low values deduced for a_h(S) are due to a reduction of the number of surfactant molecules at the interface of the nanoemulsion droplets, *i.e.*, a lower value of c_S (as with increasing dilution increasing amounts of the surfactant are monomerically dissolved). For that reason one observes for the apparent a_h only values of 0.3–0.5 nm^2 while for surfactants with such head groups as in our case one would expect values of 0.4–0.6 nm^2.[66]

3.2.2 Small-angle neutron scattering (SANS). To observe the concentration dependent structural changes of the oil–water system in more detail SANS measurements were carried out, after storing the mixed samples for ten days at 25.0 ± 0.1 °C.

The scattering curves for various water contents are depicted in Fig. 8. The intensity $I(0)$ at $q = 0$ was extrapolated by the Guinier approximation and the obtained values (Fig. 9) show a continuous increase of the scattering intensity with increasing dilution until this effect levels off at a high dilution (~80 wt% water). This demonstrates that the structural size increases with increasing dilution. It is interesting to note that for the biphasic systems the scattering intensity is always substantially lower for the lower, water-rich phase. The scattering of the upper phase connects very systematically to that of the single-phase regions, while the lower phase is mostly an excess water phase. Moreover, for the upper phase as well as for the single phase samples one observes a correlation peak (being absent only for very low and very high water content), while the lower phase shows a much lower scattering intensity with a pronounced increase at low q that may arise from dispersed oil droplets (due to incomplete phase separation) that have not yet phase separated from the lower phase (leading to q^{-4} Porod-scattering; Fig. S4†). In summary, this clearly demonstrates that in this 2-phase region

Table 2 Average molecular weight M_w, particle radius R (M_w), and surfactant head group area a_h in the nanoemulsion region (>75wt% H_2O) obtained by UV/Vis-transmittance measurements—calculated *via* eqn (20) and (21)

H_2O (%)	$M_w/10^7$ g mol^{-1}	R (M_w)/nm	a_h/nm^2
80	0.76	14.7	0.804
85	3.08	23.4	0.505
90	5.66	28.7	0.412
95	8.05	32.2	0.367
98	13.5	38.3	0.309

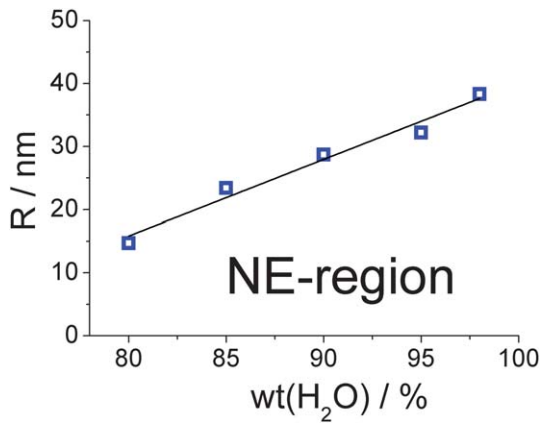

Fig. 7 Radii R (Table 2) of O/W-droplets in the nanoemulsion (NE) region from turbidity measurements, at 25.0 ± 0.1 °C in 0.5 mm cuvettes—average for R of seven different wavelengths (350, 400, 500, 600, 626, 700, 800 nm).

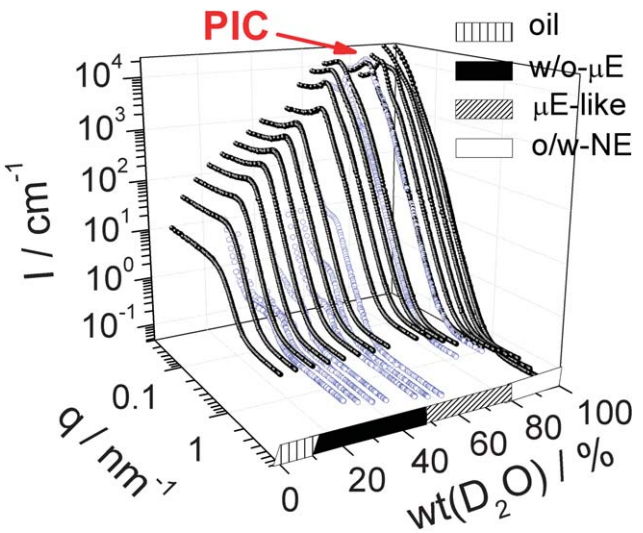

Fig. 8 SANS-measurements of the oil–water system at different D_2O contents (water conc. refers to the equivalent concentration of H_2O) after ten days of storage at 25.0 ± 0.1 °C (surfactant/oil mixture about one year old). Measurements for phase separated samples were performed only in the case of having adequate volumes available—●: upper or single Φ, ⊖: lower Φ.

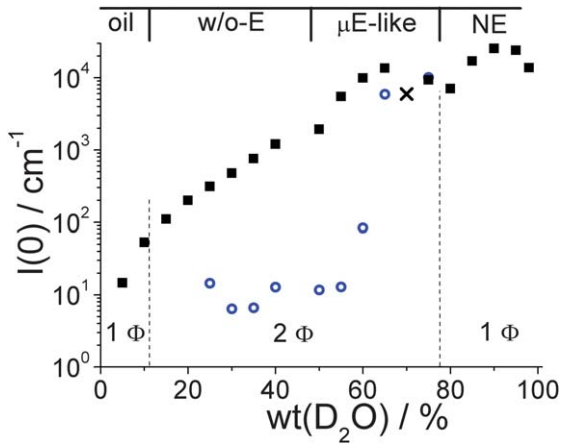

Fig. 9 Initial intensities $I(0)$ for different water conc. (values refer to H_2O)—after ten days of storage at 25.0 ± 0.1 °C. Phase separated measurements were performed only in case of having adequate volumes available. For the case of 70% D_2O it could not be avoided to measure a mixed sample, as phase separation could not be achieved (■ upper or single phase, ○ lower phase, X mixture).

the surfactant is primarily in the upper phase and forming a dense microemulsion there.

Looking at Fig. 9 it becomes obvious that, depending on the location in the phase diagram, different tendencies for the structural evolution are present. In the W/O-region (very low water concentration and upper phase) the water droplets become continuously bigger. The lower phase seems to contain small O/W-microemulsion structures (see Table S4b†) that stay more or less constant in size before becoming much bigger for concentrations beyond 60% water. Beyond this point a sponge-like microemulsion is present as evidenced by the electric conductivity (Fig. 5b) and cryo-TEM (Fig. 6). The scattering behaviour of the upper and lower phase coincides around the phase inversion concentration (PIC) (Fig. 9).

A quantitative analysis of the scattering patterns was done using the Teubner–Strey model,[35] that yields as structural parameters the domain size D_s (eqn (12)) and the correlation length ξ_i (eqn (13)) (Section 2.2.6.2). All scattering curves could be described well with this empirical model and the deduced parameters are summarised in Fig. 10 and Tables S5 and S6†. Ideally, for highly ordered systems (represented by the amphiphilicity factor f_a (Fig. 10b)), the peak position describes the domain size (alternation of oil and water phases) and the peak width is connected with the correlation length. If the evolution of the domain size D_s (Fig. 10a) is compared with a simple 3-dimensional dilution law (assuming to dilute particles of constant size for which a mean spacing D is given by eqn (22), where Φ is the volume fraction of the particles), a pronounced deviation appears shortly before the phase inversion, *i.e.*, where the nanoemulsion is formed.

$$D \approx \frac{1}{\sqrt[3]{(1-\Phi)}} \tag{22}$$

The deviations around 60–70 wt% (H_2O) (Fig. 10a and b, particularly evident for the amphiphilicity factor f_a) correlate with the formation of a bicontinuous microemulsion of high degree of ordering (Fig. 10b). Going through a bicontinuous region might be required in order to induce the phase transition—shown also by the very distinct physical behaviour (Fig. 5) in this region. The nanoemulsion formation then occurs by a phase inversion above 75% water concentration. Samples close to the phase boundary with around 75% water content vary sometimes in their appearance between single or biphasic behaviour, but the structure for the biphasic and monophasic cases is basically identical as seen from the SANS curves (Fig. 8).

In the range before phase inversion (60–75 wt% H_2O) the system shows the highest extent of ordering before further dilution leads again to more disordering caused by the growth of the nanoemulsion droplets, which was similarly observed by Gutiérrez *et al.* in the case of inversed nanoemulsions.[25]

At this point it should be noted that the obtained parameters of the Teubner–Strey model, neglecting the q^{-4} dependence at small q, of the lower phases are very similar to those of the upper

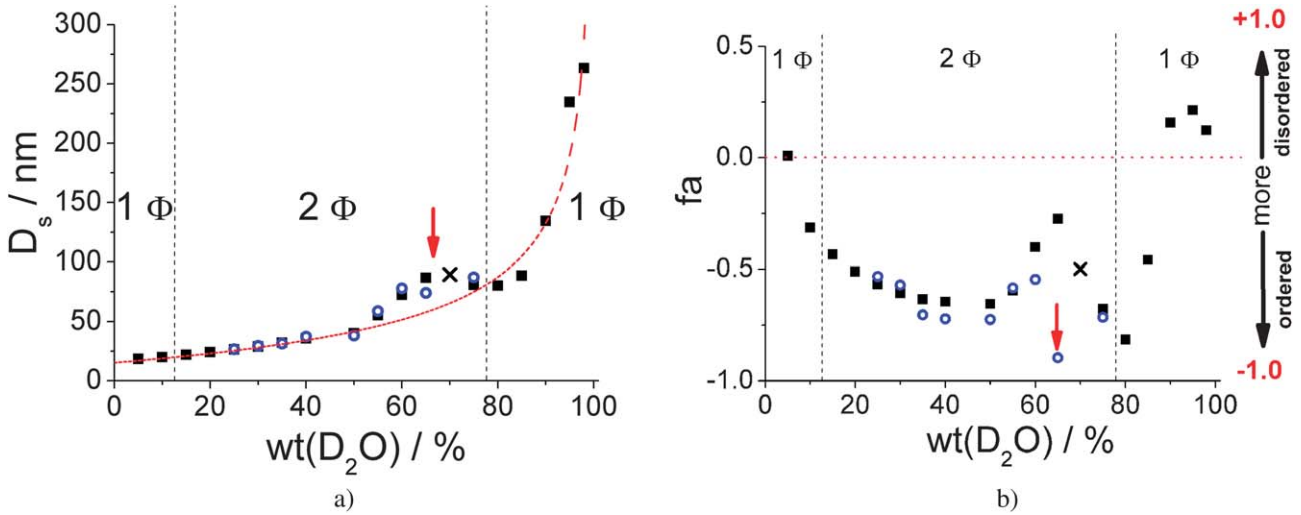

Fig. 10 Periodic distance D_s compared to a **---** 3-dim. dilution law (eqn (23)) (a) and amphiphilicity factor f_a (b) of the Teubner–Strey model as obtained from SANS as a function of water concentration (values refer to H_2O conc.). Arrows indicate the occurrence of the more ordered phase (■ upper or single phase, ○ lower phase, X mixture of two phases.)

ones, despite the fact that the scattering intensities are largely different.

The SANS spectra for the nanoemulsion range are shown in more detail in Fig. 11a and they are divided by the volume fraction of the oil/surfactant mixture. By doing so one observes that this normalised scattering intensity increases with increasing dilution. Assuming that in this range nanoemulsion droplets are present, apparently their size increases, in agreement with the observation by turbidity (Fig. 7). At low q one sees that with increasing concentration of the oil/surfactant mixture a repulsive structure factor becomes more prominent and for higher concentrations a correlation peak is observed.

For the nanoemulsions the Teubner–Strey fits show clear deviations from the experimental data as in the q-range larger than the scattering peak a distinct shoulder appears (Fig. 11b and c).

This discrepancy is not surprising as here droplet structures should be present, which are responsible for the appearance of such a shoulder and which are not well described by the Teubner–Strey model. Ideally it is applicable when bicontinuous structures are present.

Accordingly further data analysis for the nanoemulsion regime was done, using monomodal and bimodal log-normal distributions of sphere models (eqn (15)–(18)). The pronounced superiority of the bimodal model is demonstrated in Fig. 11c and Fig. S7†, where the residuals of the monomodal and bimodal fits are directly compared. Accordingly in this nanoemulsion a bimodal distribution of oil-in-water droplets is present. Close to the PIC concentration a description with the presence of just the smaller sized population is still well feasible but the importance of the larger population becomes increasingly relevant with increasing dilution (see A in Table 2). These tendencies of the bimodal distribution are best summarised in Fig. 12a which shows the size distribution functions according to the bimodal fit of the SANS data. Generally we always observe two populations, one of the smaller size distribution around $R_{1,M_w} \geq 14$–16 nm and a second somewhat bigger one with radii $R_{2,M_w} \geq 32$–40 nm. The average size increases which is due to a size increase of the individual populations (more pronounced for the larger population) and mostly due to a shift of having increasing prominence of the larger population. This increase can be explained by an increasing depletion of the surfactant from the

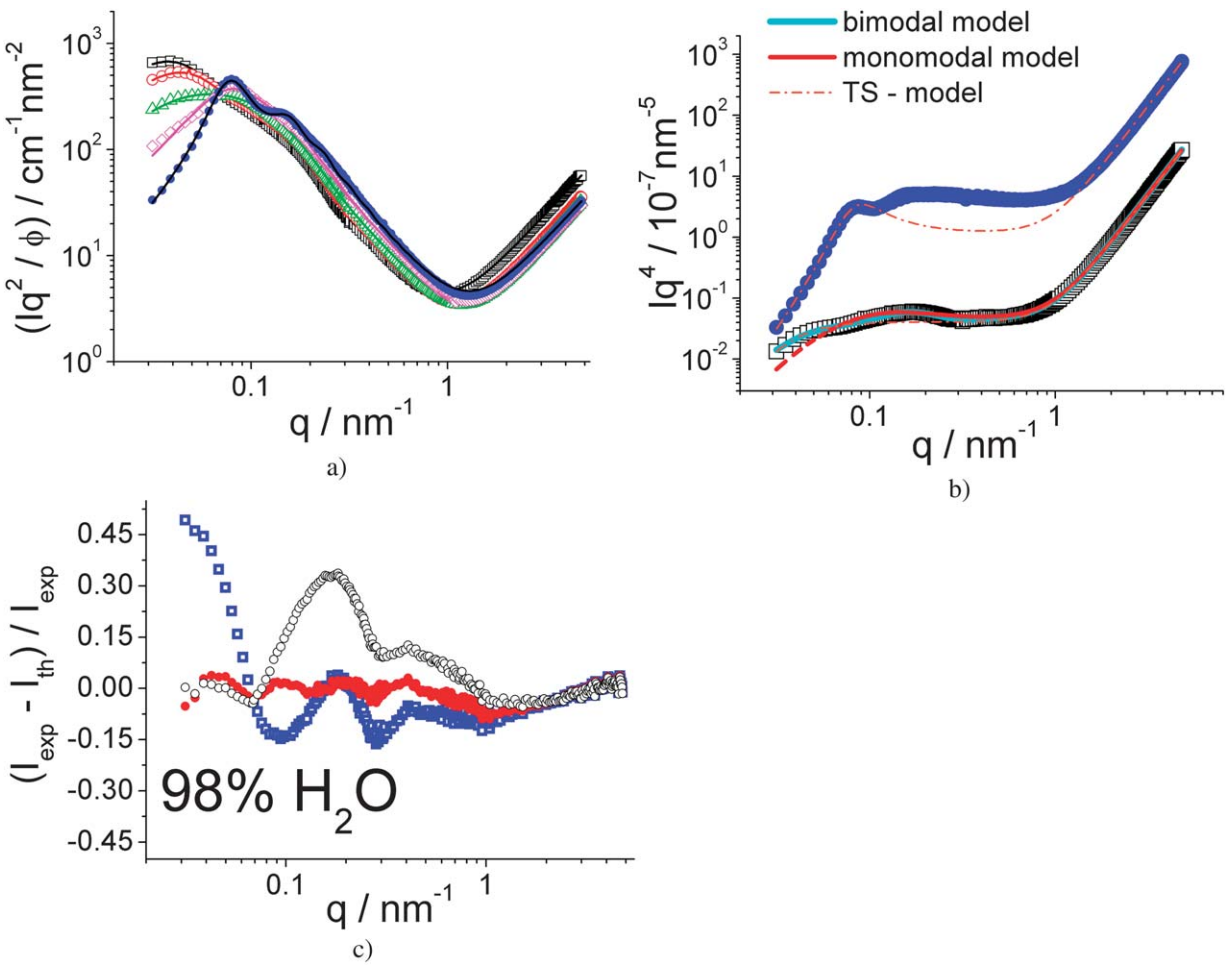

Fig. 11 (a) SANS spectra and corresponding fits, using a spherical bimodal log normal distribution with a hard sphere radius of ~39 nm upon NE-regime (□ 98%, ○ 95%, △ 90%, ◇ 85% and ● 80% H_2O), intensities are divided by the volume fraction and multiplied by q^2 for better visualisation; (b) comparison of monomodal and bimodal data-fit (98% H_2O) and demonstration of Teubner–Strey (TS) fit (80% and 98% H_2O), intensities are multiplied by q^4 for better visualisation; (c) corresponding residuals of fits for □ one and ● two populations and ○ TS-fit in the case of 98% H_2O.

nanoemulsion interface due to the dilution. With less surfactant availability for stabilising nanoemulsion droplets, they have to grow in size.

The increasing prominence of the larger size distribution is demonstrated in Fig. 12b, which shows the relative content A (by mass) contained in the droplets of the smaller size distribution. It is interesting to note that there exists an almost perfectly linear dependence of A on the concentration of water contained in the mixture.

In Fig. 13 we compare the sizes of the nanoemulsion droplets as derived from the various methods. The mean sizes of the smaller and larger population yield a lower and upper boundary for the mean particle size observed in the system. Directly after reaching the phase inversion concentration, population R_{1,M_w} is dominant (see A, Fig. 12b), while population R_{2,M_w} might be negligible at this point. According to their proportion in the mixture we can then calculate from $I(0)$ the mass-averaged mean size (X), which is increasing much more strongly due to the shift of the proportion contained in the larger and smaller population, respectively. It is very interesting to note that $R_{1/2,M_w}$ (I_0) is in a very good agreement with the radius obtained from the turbidity measurements (□ in Fig. 13), which gives further credibility to the structural picture deduced here. Accordingly we have a very self-consistent picture of having two nearby particle size distributions around 14–16 and 30–40 nm radius, which change their relative contribution with water concentration.

With the knowledge of the size distributions we could also calculate the relative ratios of the number of particles contained in size distribution 1 and 2, $N(1)/N(2)$, which is given as well in Table 3. These values as they can be directly compared to the analysis of the cryo-TEM images are discussed in the following.

3.2.3 Cryogenic transmission electron microscopy (cryo-TEM). In order to obtain complementary structural information, direct imaging of a nanoemulsion sample was done by means of cryo-TEM. The obtained images of O/W-mixture with 95% H_2O confirmed the strongly polydisperse character of this

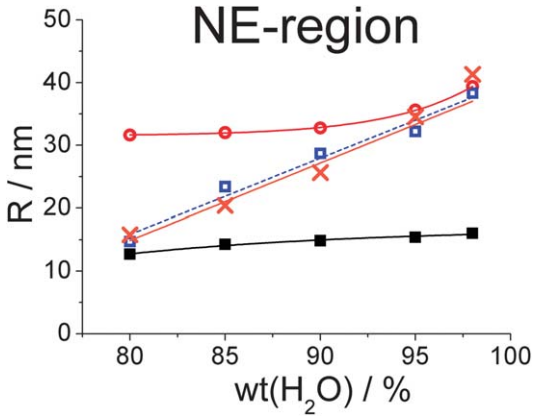

Fig. 13 Comparison of the radii determined from turbidity and SANS *via* various methods (□ R_{avg} (turbidity), ■ R_{1,M_w} (SANS), ○ R_{2,M_w} (SANS), × R_{I_0}(SANS)).

sample (*cf.* SANS-results Table 3) and an example for these TEM images is given in Fig. 14b. In order to obtain quantitative information regarding the size distribution statistical evaluations of obtained images have been accomplished through Java-based image processing (ImageJ).[67]

From this analysis based on 312 analysed droplets using six different TEM images (Fig. 14b being one example) a radii size distribution has been derived which is given in Fig. 14a. This size distribution is distinctly bimodal and shows two well-defined peaks. In Fig. 14a for a comparison we also show the number weighted log-normal size distributions of SANS data fit for the same sample. The position of the peaks coincides very well, just the scattering experiment shows a significantly broader distribution of both populations. This might be due to the fact that in scattering one sees an upper limit of the width of the size distribution, as there would be further effects like anisometry or fluctuations of the droplets that would look like polydispersity and which in our model will simply add onto the observed apparent polydispersity. However, in general the cryo-TEM

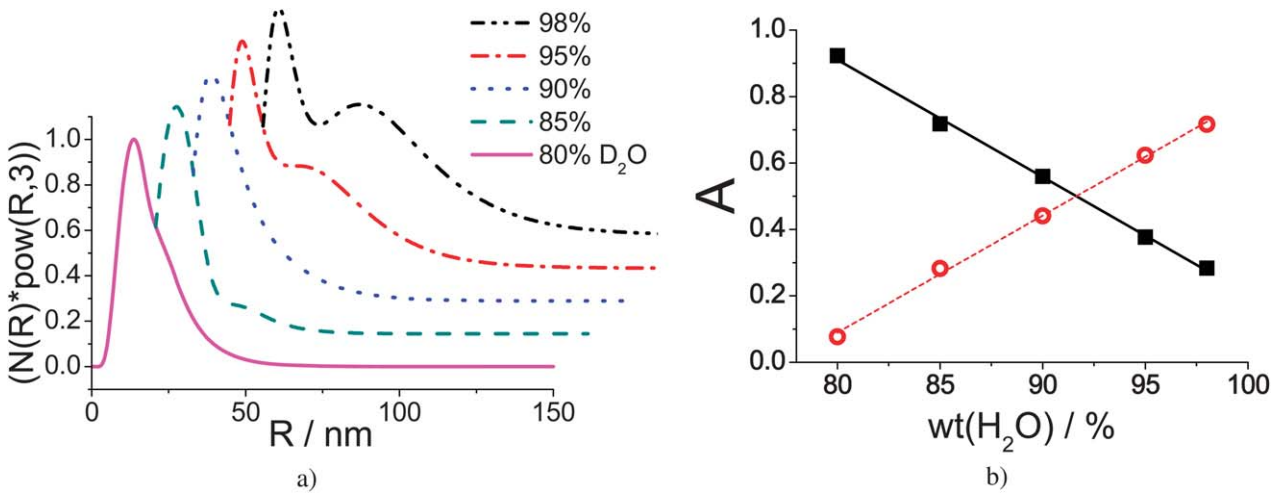

Fig. 12 (a) Standardised size distribution functions of scattering curves in the nanoemulsion region, using a bimodal log normal distributed spherical model; size distributions are depicted as number density N times the observed particle radius R to the power of three ($N(R)\cdot R^3$) *vs.* the radius R for a more pronounced visualisation of the two particle size evolutions with increasing water concentration; (b) determined amplitude of SANS-fit (*cp.* Table 3) for population ■ $R(1)$ and population ○ $R(2)$.

Table 3 Fit parameters amplitude A, mass weighted radii (number weighted radii in Table S8†) R_{1,M_w}, R_{2,M_w} and polydispersity indices σ_1 and σ_2 for populations 1 and 2, respectively; in addition mass weighted radius of both size distributions $R_{1/2,M_w}$ (I_0) and ratio N_1/N_2 of the number of droplets in population N_1 and N_2

Wt(D_2O)%	A	R_{1,M_w} nm	σ_1	R_{2,M_w} nm	σ_2	$R_{1/2,M_w}$ (I_0) nm	N_1/N_2
80	0.92	12.7	0.47	31.6	0.04	15.8	210
85	0.72	14.3	0.41	32.0	0.17	20.4	31.0
90	0.56	14.8	0.39	32.8	0.31	25.6	14.4
95	0.38	15.4	0.32	35.6	0.45	34.5	6.49
98	0.28	16.0	0.32	39.4	0.49	41.3	4.72

results demonstrate in a convincing manner that the investigated nanoemulsions contain spherical droplets with a clearly bimodal size distribution. Both methods agree very well with respect to the number-averaged mean particle sizes to be located at ~12 and ~27 nm, respectively (*e.g.* Table 3 and Table S8†). Even more impressive is the fact that the deduced ratio of the number of particles in the respective size distributions: $N(1)/N(2) \approx 6.5$ obtained from SANS is in excellent agreement with the cryo-TEM finding of $N(1)/N(2) = 6.6$ (Fig. 14).

Conclusions

An oil/surfactant/water system containing the oils, diethylhexyl carbonate, phenoxyethanol, and a parabene mixture, and as surfactant polyglyceryl-4 laurate mixed with a small amount of anionic dilauryl citrate forms spontaneously long-time stable nanoemulsions (phase separation only occurs after times longer than 6 months) by simply diluting the oil/surfactant mixture with water. The role of the dilauryl citrate is that of an electrostatic stabiliser, while the phenoxyethanol contained in the oil is a cosurfactant facilitating the high effective solubilisation capacity of the system. This process proceeds *via* the phase inversion concentration (PIC) mechanism, due to the presence of the relatively hydrophilic surfactant which becomes leached out from the emulsion droplets upon dilution.

Our observation of the phase behaviour shows that upon dilution with water this oil/surfactant system passes *via* an extended two-phase range to a homogeneous nanoemulsion phase that appears for a water content above 75%, which phase separates into an upper oil and a lower aqueous phase only after many months. At somewhat lower water content a bicontinuous structure is present, that shows a quite pronounced viscosity and conductivity maximum prior to the phase transition to the nanoemulsion phase. SANS measurements show a substantial increase in the degree of ordering while passing through the bicontinuous phase. This demonstrates that the generation of nanoemulsions is linked to the presence of a highly ordered phase in the vicinity in the phase diagram. Furthermore the very low interfacial tension of the oil/surfactant mixture explains the formation of a highly dispersed phase. Here it is interesting to note that from the interfacial tension value of 0.0175 mN m^{-1} one can estimate the droplet radius R *via* the relation:[68,69]

$$\gamma R^2 \approx kT \tag{23}$$

to be about 15 nm, which is in excellent agreement with our further structural characterisation (especially for the smaller sized population observed). It should also be noted that this size estimate is one for the maximum size of microemulsion droplets formed at the boundary of emulsification failure. However, for some interesting reason this estimate also coincides rather well with the size of our nanoemulsion.

A detailed structural investigation of the nanoemulsion region by SANS and cryo-TEM at 98 wt% water content showed that it is composed of spherical droplets with a bimodal size distribution with average sizes of $R(1) \approx 10$ and $R(2) \geq 26$ nm. A concentration dependent SANS investigation shows that directly beyond the phase transition into the nanoemulsion region, *i.e.*, at lowest dilution with water, this is dominated by the smaller O/W droplets. Generally both particle sizes are growing with increasing water concentration, but this growth is much more pronounced for the larger sized population. The growth of the

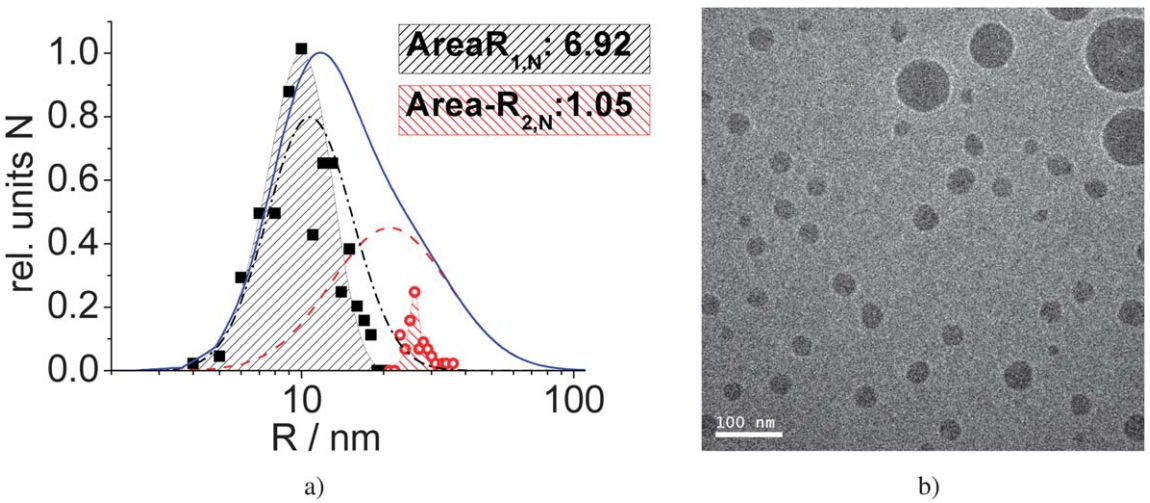

Fig. 14 (a) Normalised statistical evaluation of cryo-TEM images ((b) respectively) nanoemulsions formed at 95% H_2O (population ■ $R_{1,N}$ and ○ $R_{2,N}$); compared with number weighted (Table S6†) normalised bimodal size distribution function (a) (log normal) obtained from SANS-data fit (-·- $R_{1,N}$, --- $R_{2,N}$, — $R_{1/2,N}$).

average particle size is in good agreement for the SANS and the turbidity data and one observes a roughly linear increase of size with the water content in the mixture. This growth is due to the fact that upon dilution the hydrophilic surfactant partitions increasingly into the aqueous phase and therefore less surfactant is available to cover the emulsion droplets, which therefore have to increase in size. With increasing water content the proportion of the smaller particles ($N(1)$) decreases in favour of the formation of the bigger droplets ($N(2)$). Using SANS and cryo-TEM imaging yields a reliable picture of this situation and both methods are in excellent agreement with respect to the relative amounts of particles present in the form of larger and smaller droplets. This bimodal size distribution might be the result of an initial Ostwald ripening of the system that becomes arrested in an early stage. In any case due to the rather high solubility of the oils contained one would expect a rather fast Ostwald ripening in our nanoemulsion but apparently this is effectively suppressed. The reason for this remarkable stability is not yet clear, but will be the focus of future studies.

Therefore our investigation demonstrates that the nanoemulsion studied here is in reality composed of a bimodal distribution of somewhat differently sized droplets with mean radii in the range of 15 or 30–40 nm, respectively. The smaller droplet size is consistent with the size expected for microemulsion droplets. This means that here one may have a situation where microemulsion droplets coexist with larger sized, metastable emulsion droplets. This is a new insight into the structural details of PIC nanoemulsions, which should be important for the future developments of these interesting systems. This knowledge will be important for the rational design of nanoemulsions and for their further applications.

Acknowledgements

The author is grateful to the ILL for doctoral scholarship through the ILL PhD program and allocated beamtime. Furthermore P.H. thanks R. Schweins for his help during SANS-data analysis. Katharina Bressel and Michael Muthig are acknowledged for their very valuable help with the modelling of the fit curves. M. Gradzielski would like to thank the Institute Laue-Langevin (ILL, Grenoble, France) and the DFG (project GR1030/10) for hospitality and funding of his sabbatical stay during which a larger part of this manuscript was produced. Furthermore we want to thank C. Solans for fruitful discussions. Moreover we are grateful for the financial support by the German Academic Exchange Program (DAAD), which allowed us a fruitful cooperation with the group of N. J. Wagner at the University of Delaware (USA) where some of the investigations have been done (particularly the cryo-TEM measurements).

Notes and references

1 T. F. Tadros and B. Vincent, *Encyclopedia of Emulsion Technology*, Marcel Dekker, New York, 1983.
2 P. Taylor, *Adv. Colloid Interface Sci.*, 1998, **75**, 107–163.
3 H. Nakajima, *Industrial Applications of Microemulsions*, Marcel Dekker, New York, 1997, vol. 66, pp. 175–197.
4 M. S. El-Aasser and E. D. Sudol, *JCT Res.*, 2004, **1**, 21–31.
5 C. Solans, P. Izquierdo, J. Nolla, N. Azemar and M. J. Garcia-Celma, *Curr. Opin. Colloid Interface Sci.*, 2005, **10**, 102–110.
6 T. F. Tadros, P. Izquierdo, J. Esquena and C. Solans, *Adv. Colloid Interface Sci.*, 2004, **108**, 303–318.
7 K. Buszello and B. W. Müller, *Pharmaceutical Emulsions and Suspensions*, Marcel Dekker, New York, 2000, pp. 191–228.
8 P. Walstra, *Encyclopedia of Emulsion Technology*, Marcel Dekker, New York, 1983, pp. 57–127.
9 P. Walstra and P. E. A. Smoulders, *Modern Aspects of Emulsion Science*, The Royal Society of Chemistry, Cambridge, 1998.
10 R. W. Wood, *Philos. Mag.*, 1927, **4**, 417–436.
11 H. Schubert and S. Brösel, *Chem. Eng. Process.*, 1999, **38**, 533–540.
12 S. Benita and M. Y. Levy, *J. Pharm. Sci.*, 1993, **82**, 1069–1079.
13 S. Tomomasa, M. Kochi and H. Nakajima, *J. Jpn. Oil Chem.*, 1988, **37**, 1012.
14 E. D. Sudol and M. S. El-Aasser, *Emulsion Polymerization and Emulsion Polymers*, John Wiley & Sons Ltd., Chichester, UK, 1997, pp. 700–722.
15 K. Shinoda and Y. Shibata, *Colloids Surf.*, 1986, **19**, 185–196.
16 A. Wadle, T. Förster and W. von Rybinski, *Colloids Surf., A*, 1993, **76**, 51–57.
17 K. Shinoda and H. Saito, *J. Colloid Interface Sci.*, 1968, **26**, 70–74.
18 K. Shinoda and H. Saito, *J. Colloid Interface Sci.*, 1969, **30**, 258–263.
19 M. Minana-Perez, C. Gutron, C. Zundel, J. M. Anderez and J. L. Salager, *J. Dispersion Sci. Technol.*, 1999, **20**, 893–905.
20 S. Lamaallam, H. Bataller, C. Dicharry and J. Lachaise, *Colloids Surf., A*, 2005, **270**, 44–51.
21 W. R. Liu, D. J. Sun, C. F. Li, Q. Liu and H. Xu, *J. Colloid Interface Sci.*, 2006, **303**, 557–563.
22 C. Solans, P. Izquierdo, J. Nolla, N. Azemar and M. J. Garcia-Celma, *Curr. Opin. Colloid Interface Sci.*, 2005, **10**, 102–110.
23 N. Sadurní, C. Solans, N. Azemara and M. J. García-Celma, *Eur. J. Pharm. Sci.*, 2005, **26**, 438–445.
24 D. Morales, J. M. Gutiérrez, M. J. García-Celma and Y. C. Solans, *Langmuir*, 2003, **19**, 7196–7200.
25 M. Porras, C. Solans, C. Gonzáles, A. Martínez, A. Guinart and J. M. Gutiérrez, *Colloids Surf., A*, 2004, **249**, 115–118.
26 M. Porras, C. Solans, C. Gonzalez and J. M. Gutierrez, *Colloids Surf., A*, 2008, **324**, 181–188.
27 I. Solè, A. Maestro, C. M. Pey, C. González, C. Solans and J. M. Gutierrez, *Colloids Surf., A*, 2006, **288**, 144–150.
28 A. Maestro, I. Solè, C. González, C. Solans and J. M. Gutiérrez, *J. Colloid Interface Sci.*, 2008, **327**, 433–439.
29 J. Meyer, G. Polak and R. Scheuermann, *Cosmet. Toiletries*, 2007, **122**, 63–68.
30 B. Jacrot, *Rep. Prog. Phys.*, 1976, **39**, 911–953.
31 U. Keiderling, *Appl. Phys. A: Mater. Sci. Process.*, 2002, **74**, 1455–1457.
32 http://www.ncnr.nist.gov/resources/sldcalc.html, 09.06.2009.
33 A. Guinier and G. Fournet, *Small Angle Scattering of X-Rays*, John Wiley, New York, 1955.
34 O. Spalla, *Neutrons, X-rays and Light: Scattering Methods Applied to Soft Condensed Matter*, Elsevier, North-Holland, 2002.
35 M. Teubner and R. Strey, *J. Chem. Phys.*, 1987, **87**, 3195–3200.
36 P. Debye, H. R. Anderson and H. Brumberger, *J. Appl. Phys.*, 1957, **28**, 679–683.
37 K.-V. Schubert and R. Strey, *J. Chem. Phys.*, 1991, **95**, 8532–8545.
38 K.-V. Schubert, R. Strey, S. R. Kline and E. W. Kaler, *J. Chem. Phys.*, 1994, **101**, 5343–5355.
39 M. Gradzielski, D. Langevin, T. Sottmann and R. Strey, *J. Chem. Phys.*, 1996, **104**, 3782–3787.
40 M. Schick and W. H. Shih, *Phys. Rev. Lett.*, 1987, **59**, 1205–1208.
41 J. A. Silas and E. W. Kaler, *J. Colloid Interface Sci.*, 2003, **257**, 291–298.
42 N. W. Ashcroft and J. Lekner, *Phys. Rev.*, 1966, **145**, 83–90.
43 O. Faust, *Kolloid-Z.*, 1927, **41**, 54–55.
44 H. Hoffmann, C. Thunig, U. Munkert, H. W. Meyer and W. Richter, *Langmuir*, 1992, **8**, 2629–2638.
45 O. Diat and D. Roux, *Langmuir*, 1995, **11**, 1392–1395.
46 H. Pleiner and H. R. Brand, *Europhys. Lett.*, 1991, **15**, 393–397.
47 T. Engels, T. Förster and W. von Rybinski, *Colloids Surf., A*, 1995, **99**, 141–149.
48 T. Förster, W. von Rybinski and A. Wadle, *Adv. Colloid Interface Sci.*, 1995, **58**, 119–149.
49 C. Solans, J. Esquena, A. M. Forgiarini, N. Usón, D. Morales, P. Izquierdo, N. Azemar and M. J. García-Celma, *Surfactant in Solution: Fundamental and Applications*, Marcel Dekker, New York, 2002.

50 S. Gasic, B. Jovanovic and S. Jovanovic, *J. Serb. Chem. Soc.*, 2002, **67**, 31–39.
51 H. J. Yang, W. G. Cho and S. N. Park, *J. Ind. Eng. Chem.*, 2009, **15**, 331–335.
52 J. Allouche, E. Tyrode, V. Sadtler, L. Choplin and J. L. Salager, *Langmuir*, 2004, **20**, 2134–2214.
53 A. Forgiarini, J. Esquena, C. González and C. Solans, *Prog. Colloid Polym. Sci.*, 2001, **118**, 184–189.
54 P. Izquierdo, J. Esquena, Th. F. Tadros, C. Dederen, M. J. Garcia, N. Azemar and C. Solans, *Langmuir*, 2002, **18**, 26–30.
55 T. Sottmann and R. Strey, *J. Chem. Phys.*, 1997, **106**, 8606–8615.
56 K. Shinoda and H. Kunieda, *J. Colloid Interface Sci.*, 1973, **42**, 381–387.
57 P. Fernandez, V. André, J. Rieger and A. Kühnle, *Colloids Surf., A*, 2004, **251**, 53–58.
58 N. Usón, M. J. Garcia and C. Solans, *Colloids Surf., A*, 2004, **250**, 415–421.
59 J. M. Gutiérrez, A. Maestro, I. Solè, C. M. Pey and J. Nolla, *Curr. Opin. Colloid Interface Sci.*, 2008, **13**, 245–251.
60 L. Wang, R. Tabor, J. Eastoe, X. Li, R. K. Heenan and J. Dong, *Phys. Chem. Chem. Phys.*, 2009, **11**, 9772–9778.
61 R. Strey, *Colloid Polym. Sci.*, 1994, **272**, 1005–1019.
62 D. Quemada and D. Langevin, *J. Theor. Appl. Mech. Numero Spec.*, 1985, **SI**, 201–237.
63 M. Gradzielski and H. Hoffmann, *Handbook of Microemulsion Science and Technology*, Marcel Dekker, New York, 1999, pp. 357–386.
64 Z. J. Yu and R. D. Neuman, *Langmuir*, 1995, **11**, 1081–1086.
65 P. C. Hiemenz and R. Rajagopalan, *Principles of Colloid and Surface Chemistry*, CRC Taylor&Francis, Boca Raton, 3rd edn, 1997.
66 M. J. Rosen, *Surfactants and Interfacial Phenomena*, Wiley-Interscience, 3rd edn, 2004.
67 M. D. Abràmoff, P. J. Magãlhaes and S. J. Ram, *Biophotonics International*, 2004, **11**, 36–42.
68 M. L. Robbins, J. Bock and J. S. Huang, *J. Colloid Interface Sci.*, 1988, **126**, 114–133.
69 M. Gradzielski, D. Langevin and B. Farago, *Phys. Rev. E: Stat. Phys., Plasmas, Fluids, Relat. Interdiscip. Top.*, 1996, **53**, 3900–3919.